PHYSICAL REVIEW E **107**, 065204 (2023)

Investigation on the near-field cutoff effect in a subwavelength plasma shell with near-zero permittivity

Peiqi Chen,[1] Qiuyue Nie,[1,2,*] Shu Lin,[3] Liang Qian,[4] Zhonglin Zhang,[2] Xiaogang Wang,[2,4]
Zhuotao Meng,[1] and Guoqiang Wei[4]
[1]*School of Electrical Engineering and Automation, Harbin Institute of Technology, Harbin 150001, China*
[2]*Laboratory for Space Environment and Physical Science, Harbin Institute of Technology, Harbin 150001, China*
[3]*School of Electronics and Information Engineering, Harbin Institute of Technology, Harbin 150001, China*
[4]*School of Physics, Harbin Institute of Technology, Harbin 150001, China*

(Received 15 December 2022; accepted 9 May 2023; published 12 June 2023)

Although the plasma-induced receiving and radiating near-field cutoff phenomena in the subwavelength regime are found of crucial importance in electromagnetic (EM) signal transmissions and plasma property studies, their mechanisms to a large extent remain unclear and undistinguished. In this paper, in the perspective of field and energy transfer, it is demonstrated that the cutoff in the near-field regime is completely different from that in the geometric optical regime. Results show that, for the receiving mode, epsilon-near-zero (ENZ) plasmas can be treated as a nearly ideal EM fluid, and thus, EM waves are restricted into the plasma channel. For the radiating mode, on the other hand, it is the destructive interference between the electric dipole fields of the antenna and the ENZ plasma that results in vanishing far-field radiation. As an important supplement to the existing cutoff theories, our results not only offer clearer physical insights into the near-field cutoff effect but also provide a helpful reference for cutoff-related practical applications in various frequency bands.

DOI: 10.1103/PhysRevE.107.065204

I. INTRODUCTION

As a counterpart of noble metals in the visible light regime, nonmagnetized low-temperature gaseous plasmas have shown great potential in the microwave regime for advanced electromagnetic (EM) manipulation, including waveguides [1,2], filters [3,4], antennas [5,6], and invisible cloaks [7], and have attracted increasing attention in the past two decades. One of the research highlights is to extend the characteristic scale of interaction between plasmas and EM waves into the subwavelength regime, where the smallest length scale of the plasma is less than the typical EM wavelength. In this regime, EM properties of plasmas become quite distinct from that of the bulk. Take cutoff phenomena as an example in EM signal transmissions and plasma property studies. In general, the dispersion relation of high-frequency optical EM waves propagating in unmagnetized plasmas is given by [8]

$$\omega^2 = \omega_{\mathrm{pe}}^2 + k^2 c^2, \tag{1}$$

where ω is the angular frequency of the EM wave, ω_{pe} is the plasma frequency, k is the wave number in plasmas, and c is the speed of light in vacuum. It can be seen easily that, for overdense plasmas, namely, $\omega_{\mathrm{pe}} > \omega$, k^2 becomes negative, resulting in the EM wave amplitude decaying exponentially in a distance of $\sim 1/|k|$. The wave is then reflected by the surface of plasmas. Therefore, $\omega = \omega_{\mathrm{pe}}$ is also known as the cutoff frequency, and the corresponding electron density is called the critical density. The cutoff condition is thus given by $k = 0$. The physical insight of such a cutoff is very clear. For $\omega_{\mathrm{pe}} < \omega$, the wave energy, characterized by the frequency ω, is partially used to excite the plasma oscillation, characterized by ω_{pe}, while the rest can still propagate in the plasma with a wave number k. For $\omega_{\mathrm{pe}} = \omega$, the wave energy is totally used to excite the plasma oscillation with nothing left for further propagation. For $\omega_{\mathrm{pe}} > \omega$, however, in addition to the plasma oscillation, the wave can still penetrate the overdense plasma in an exponentially decayed evanescent form, as $\sim e^{-|k|x}$. Nevertheless, the skin depth ($\sim 1/|k|$) is much less than the typical spatial length of the plasma and thus approximately ignored. For spatially nonuniform plasmas, in the geometric optical approximation where the spatial scale is much longer than the EM wavelength, the cutoff condition is also characterized by $k = 0$, where $k = dS/dx$, with x along the transmission direction and S the eikonal function. The physical insight of the cutoff in such nonuniform plasmas is the same as that in the approximately uniform plasmas, as discussed above. The cutoff phenomena have then been widely investigated in various fields, such as plasma density diagnosis [9–11], radar detection [12,13], and wireless communication [14]. Nevertheless, in the subwavelength regime, the geometric optical approximation is no longer valid, and particularly the skin depth is on the same order or even much longer than the plasma size. The wave propagation is thus no longer vanished in the overdense region ($\omega_{\mathrm{pe}} > \omega$) but penetrated through the subwavelength plasma. New features may then appear. For example, an EM wave can partially pass through an overdense plasma slab with a thickness that is thinner than the electron skin depth [15]. Also, it has been demonstrated that EM waves can perfectly tunnel through subwavelength channels with near-zero permittivity [epsilon-near-zero (ENZ)] [16,17]. Moreover, for enclosed

---

[*] Corresponding author: nieqiuyue@hit.edu.cn

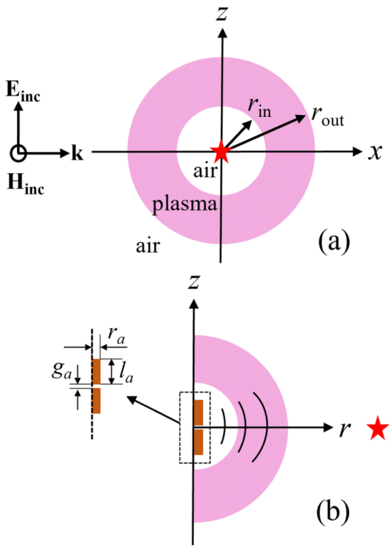

FIG. 1. Schematics of a uniform subwavelength plasma shell in the (a) receiving mode [the $x-z$ cross-section of a three-dimensional (3D) model with $y = 0$], and (b) radiating mode [the $r-z$ cross-section of a simplified two-dimensional (2D) axisymmetric model with $\varphi = 0$].

subwavelength plasmas where the near-field effect plays an important role, e.g., a plasma shell, cutoff can be reshaped due to the existence of localized modes, referred to the near-field cutoff effect hereafter. As a result, receiving and radiating efficiencies of an electrically small antenna (ESA) modulated by a subwavelength plasma shell exhibit a Fano-like line shape [5,18–22] as $\omega_{\rm pe}$ increases. Particularly, experimental results have shown that, different from the cutoff effect in the geometric optical regime where the wave is almost vanished in the entire $\omega_{\rm pe} > \omega$ region, the receiving and radiating efficiencies in the near-field scenarios only reach a local minimum at $\omega = \omega_{\rm pe}$ [5,9,18,21,22]. Concerning the mechanisms of the near-field cutoff effect, existing analyses are mainly based on the geometric optical approximation, which is invalid in subwavelength circumstances. Although electric circuit models [23,24] may provide a macroscopic picture of the near-field cutoff effect, clearer and deeper physical insight is still desirable. Also, the difference between receiving and radiating near-field cutoffs remains unexplored. Therefore, the focus of this paper is to make a comprehensive and in-depth investigation on the mechanisms of near-field cutoff effect, particularly from the perspective of field and energy transfer.

II. SIMULATION MODEL

In this paper, a uniform but subwavelength plasma shell, as shown in Fig. 1, is applied to investigate the mechanism of the near-field cutoff by full-wave finite element simulations (COMSOL Multiphysics [25], version 5.6). Here, the inner and outer radii of the plasma shell are $r_{\rm in}$ and $r_{\rm out}$, respectively, and the background medium, inside and outside the shell, is air. Also, the relative complex permittivity of plasma is given by (a time dependence of oscillation, $e^{j\omega t}$, is assumed)

$$\varepsilon_{\rm p}(\omega, \omega_{\rm pe}) = 1 - \frac{\omega_{\rm pe}^2}{\omega^2 + \nu^2} - i\frac{\omega_{\rm pe}^2 \nu}{\omega(\omega^2 + \nu^2)} = \varepsilon'_{\rm p} - i\varepsilon''_{\rm p}, \quad (2)$$

where v is the collision frequency. Note that the plasma shell operates in two modes, namely, receiving [Fig. 1(a)] and radiating modes [Fig. 1(b)]. For the former, the $x-z$ cross-section of a three-dimensional (3D) model ($y = 0$) is schematically shown in Fig. 1(a), where the plasma is illuminated by an incident plane wave, propagating along the x axis with a z-polarized electric component. To evaluate the receiving characteristics, we defined the receiving gain ($G_{\rm rec}$) based on the norm of electric field at the center of the shell [$\mathbf{E}$(0,0,0), as indicated by the red star in Fig. 1(a)]:

$$G_{\rm rec} = 20\log_{10}\left(\frac{|\mathbf{E}_{\rm wp}(0,0,0)|}{|\mathbf{E}_{\rm np}(0,0,0)|}\right), \quad (3)$$

where the subscript wp designates with the plasma shell, and np means without the plasma shell. For the latter, considering cylindrical symmetry, the $r-z$ cross-section ($\varphi = 0$) of a simplified two-dimensional (2D) axisymmetric model is shown in Fig. 1(b), in which the plasma oscillation is excited by a coaxially fed ESA located at the center of the shell. Moreover, the arm length, radius, and feed gap of the ESA are l_a, r_a, and g_a, respectively. Like $G_{\rm rec}$, radiating gain ($G_{\rm rad}$) is defined as

$$G_{\rm rad} = 20\log_{10}\left(\frac{|\mathbf{E}_{\rm wp}(\lambda/4,0)|}{|\mathbf{E}_{\rm np}(\lambda/4,0)|}\right), \quad (4)$$

where λ is the wavelength of EM waves in vacuum. Note that the testing point (λ/4,0), as marked by the red star in Fig. 1(b), situates at the far field of the ESA (by $\lambda/4 > \lambda/2\pi$).

III. RESULTS AND DISCUSSION

Without loss of generality, we studied a typical case in microwave communication with the frequency of the incident EM wave and the operating frequency of the ESA both setting as 1 GHz, and the plasma is weakly collisional with $v = 0.1$ GHz. Additionally, the plasma shell is of subwavelength with $r_{\rm in} = 1$ cm and $r_{\rm out} = 2$ cm ($r_{\rm out}/\lambda_{\rm 1GHz} = \frac{1}{15} \ll 1$). As for the ESA, $l_a = 0.3$ cm, $r_a = l_a/20$, $g_a = l_a/100$, and averaged input power is 1 W. On this basis, receiving ($G_{\rm rec}$) and radiating ($G_{\rm rad}$) gains under different normalized plasma frequencies ($\omega_{\rm pe}/\omega_{\rm 1GHz}$) varying from 0 to 1.1 are shown in Fig. 2. It can be observed that $G_{\rm rec}$ and $G_{\rm rad}$ perfectly coincide with each other, consistent with the reciprocity theorem of passive media. Moreover, different from the cutoff effect of bulky plasmas, $G_{\rm rec}$ and $G_{\rm rad}$ simultaneously reach a local minimum or exhibit an antiresonance line shape around $\omega_{\rm pe}/\omega_{\rm 1GHz} = 1$.

A. Receiving mode

The physical insights of receiving and radiating features of near-field cutoffs are then analyzed. For the receiving mode, the distributions of electric field ($\mathbf{E}$) and time-averaged Poynting flux ($\mathbf{P}_{\rm av}$), where plasma frequency is less than ($\omega_{\rm pe}/\omega_{\rm 1GHz} = 0.8083$), near ($\omega_{\rm pe}/\omega_{\rm 1GHz} = 1.0022$), or larger than ($\omega_{\rm pe}/\omega_{\rm 1GHz} = 1.0665$) the cutoff frequency, are shown in Figs. 3 and 4, respectively. For $\mathbf{E}$, it can be observed in Fig. 3(b) that the electric field is mostly distributed in the plasma shell when $\omega_{\rm pe}/\omega_{\rm 1GHz} = 1.0022$, which gives rise to the cutoff in the receiving mode. By contrast, in the vicinity a bit far from the cutoff frequency, the electric field partially crosses through the inner boundary of the plasma shell and

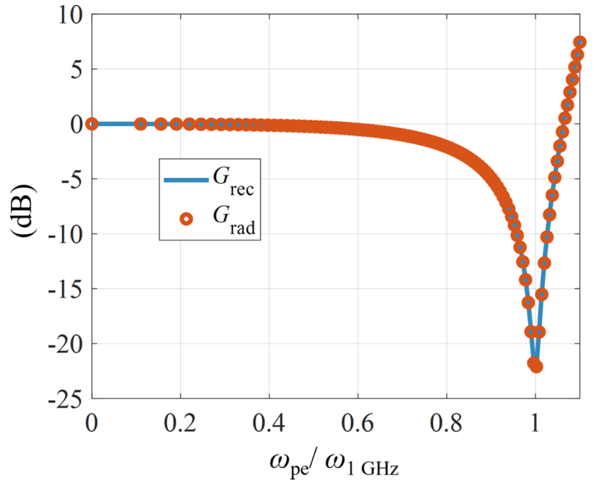

FIG. 2. Receiving (G_{rec}) and radiating (G_{rad}) gains under different $\omega_{\mathrm{pe}}/\omega_{1\mathrm{GHz}}(0 \leqslant \omega_{\mathrm{pe}}/\omega_{1\mathrm{GHz}} \leqslant 1.1)$.

gets into the central air region, and thus, the cutoff is undermined, as shown in Figs. 3(a) and 3(c). The cutoff picture is much clearer for $\mathbf{P}_{\mathrm{av}}$ distribution. Specifically, the flux is squeezed into the plasma shell with no leaking to the central region, in the cutoff of $\omega_{\mathrm{pe}}/\omega_{1\mathrm{GHz}} = 1.0022$ [Fig. 4(b)]. To the other cases a bit away from the cutoff, the energy flux partially leaks into the central region to break the cutoff. Of particular interest is that the streamline of $\mathbf{P}_{\mathrm{av}}$ exhibits a detour effect in the plasma shell to create a cloaking effect for the central region, when $\omega_{\mathrm{pe}}/\omega_{1\mathrm{GHz}} = 1.0022$, as shown in Fig. 4(b). The flux detour effect is clearly reduced in the other two cases of $\omega_{\mathrm{pe}}/\omega_{1\mathrm{GHz}} = 0.8083$ and 1.0665, as shown in Figs. 4(a) and 4(c).

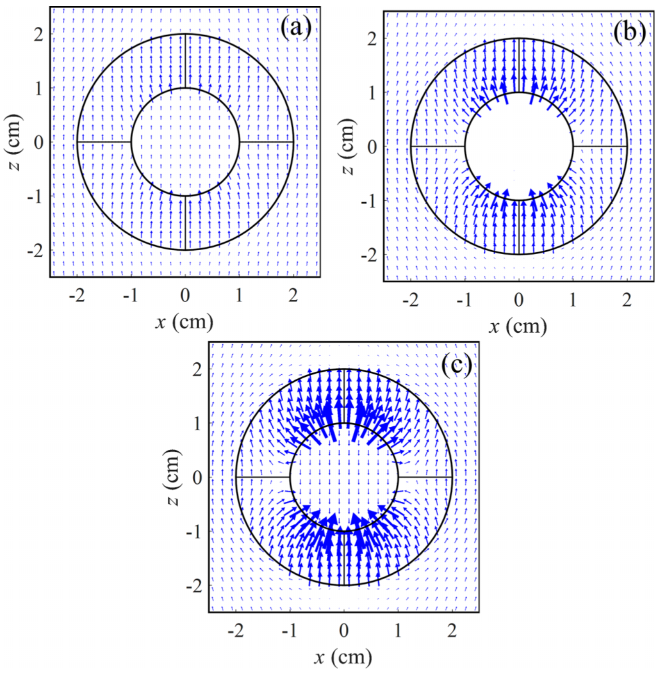

FIG. 3. Distributions of electric field $\mathbf{E}$ in the $x-z$ plane for the receiving mode with (a) $\omega_{\mathrm{pe}}/\omega_{1\mathrm{GHz}} = 0.8083$, (b) $\omega_{\mathrm{pe}}/\omega_{1\mathrm{GHz}} = 1.0022$, and (c) $\omega_{\mathrm{pe}}/\omega_{1\mathrm{GHz}} = 1.0665$.

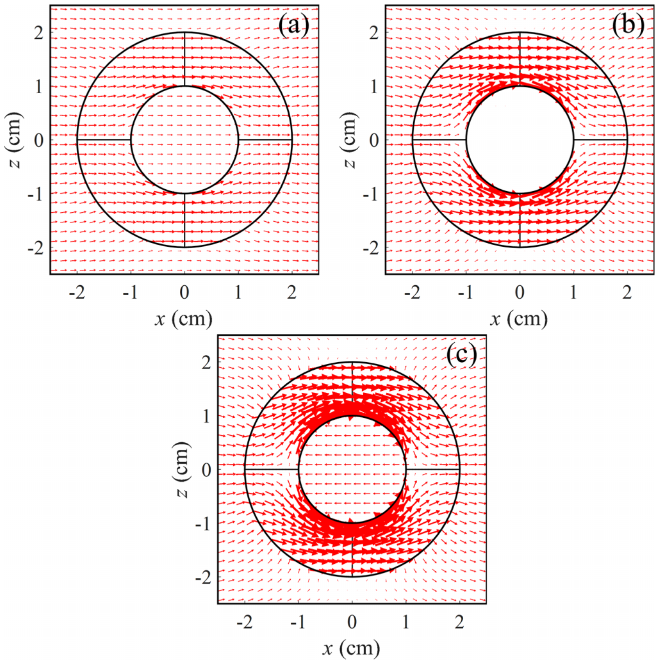

FIG. 4. Distributions of the time-averaged Poynting flux $\mathbf{P}_{\mathrm{av}}$ in the $x-z$ plane for the receiving mode with (a) $\omega_{\mathrm{pe}}/\omega_{1\mathrm{GHz}} = 0.8083$, (b) $\omega_{\mathrm{pe}}/\omega_{1\mathrm{GHz}} = 1.0022$, and (c) $\omega_{\mathrm{pe}}/\omega_{1\mathrm{GHz}} = 1.0665$.

Further, considering that the simulation model is symmetric along the y direction, we defined the t- (time-) and y-averaged complex Poynting vector in the $x-z$ plane, namely, $\tilde{\mathbf{P}}_{(x-z)}$, by the y-averaged electric ($\tilde{\mathbf{E}}$) and magnetic ($\tilde{\mathbf{H}}$) fields, written as

$$\tilde{\mathbf{P}}_{(x-z)} = \frac{\tilde{\mathbf{E}} \times \tilde{\mathbf{H}}^*}{2}, \tag{5}$$

where $\tilde{\mathbf{E}} = \int_y \mathbf{E}dy$ and $\tilde{\mathbf{H}} = \int_y \mathbf{H}dy$. Then the divergence and curl of $\tilde{\mathbf{P}}_{(x-z)}$ in the plasma shell are given by

$$\nabla \cdot \tilde{\mathbf{P}}_{(x-z)} = -\frac{\omega}{2}\varepsilon_0\varepsilon_{\mathrm{p}}''|\tilde{\mathbf{E}}|^2 + \frac{i\omega}{2}(\varepsilon_0\varepsilon_{\mathrm{p}}'|\tilde{\mathbf{E}}|^2 - \mu_0|\tilde{\mathbf{H}}|^2), \tag{6}$$

$$\nabla \times \tilde{\mathbf{P}}_{(x-z)} = \tfrac{1}{2}[(\tilde{\mathbf{H}}^* \cdot \nabla)\tilde{\mathbf{E}} - (\tilde{\mathbf{E}} \cdot \nabla)\tilde{\mathbf{H}}^* + \tilde{\mathbf{E}}(\nabla \cdot \tilde{\mathbf{H}}^*) - \tilde{\mathbf{H}}^*(\nabla \cdot \tilde{\mathbf{E}})]. \tag{7}$$

It should be noted that the real ($\varepsilon_{\mathrm{p}}'$) and imaginary ($\varepsilon_{\mathrm{p}}''$) parts of the relative plasma permittivity vanish when $\omega_{\mathrm{pe}}/\omega_{1\mathrm{GHz}} \sim 1$, where the plasma is then equivalent to an ENZ medium. In such a situation, since $\varepsilon_{\mathrm{p}}'' \to 0$, $\mathrm{Re}(\nabla \cdot \tilde{\mathbf{P}}_{(x-z)}) \to 0$. Also, according to Eq. (7), $\nabla \times \tilde{\mathbf{P}}_{(x-z)} = \mathbf{0}$ due to the following three reasons [26]: (1) the ENZ plasma is passive, and thus, $\nabla \cdot \tilde{\mathbf{E}} = 0$ and $\nabla \cdot \tilde{\mathbf{H}} = 0$ (excluding boundaries); (2) as $\tilde{E}_y = \int_y E_y dy = 0$, by $\tilde{\mathbf{E}} = \hat{x}\tilde{E}_x + \hat{z}\tilde{E}_z$ and $\tilde{\mathbf{H}} = \hat{y}\tilde{H}_y$, then $(\tilde{\mathbf{H}}^* \cdot \nabla)\tilde{\mathbf{E}}$ must be vanished; and (3) by $\tilde{\mathbf{E}} = \nabla\tilde{H}_y \times \hat{y}/(i\omega\varepsilon_0\varepsilon_{\mathrm{p}})$, $\tilde{H}_y$ in the ENZ plasma shell should be a constant to prevent the divergence of the electric field, and thus, $(\tilde{\mathbf{E}} \cdot \nabla)\tilde{\mathbf{H}}^*$ also makes no distribution to the curl of $\tilde{\mathbf{P}}_{(x-z)}$. Based on the above discussion, the ENZ plasma can be approximately regarded as an ideal EM fluid [26], where $\tilde{\mathbf{P}}_{(x-z)}$ and $\tilde{\mathbf{E}}$ are parallel and

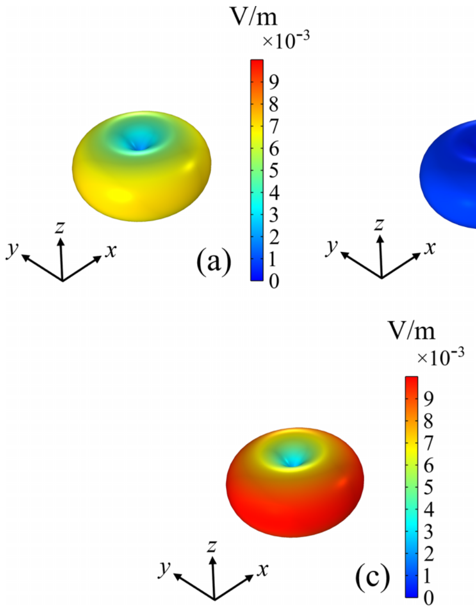

FIG. 5. Three-dimensional (3D) scattering patterns, in the norm of the electric far field, for the radiating mode, with (a) $\omega_{\text{pe}}/\omega_{1\text{GHz}} = 0.8083$, (b) $\omega_{\text{pe}}/\omega_{1\text{GHz}} = 1.0022$, or (c) $\omega_{\text{pe}}/\omega_{1\text{GHz}} = 1.0665$.

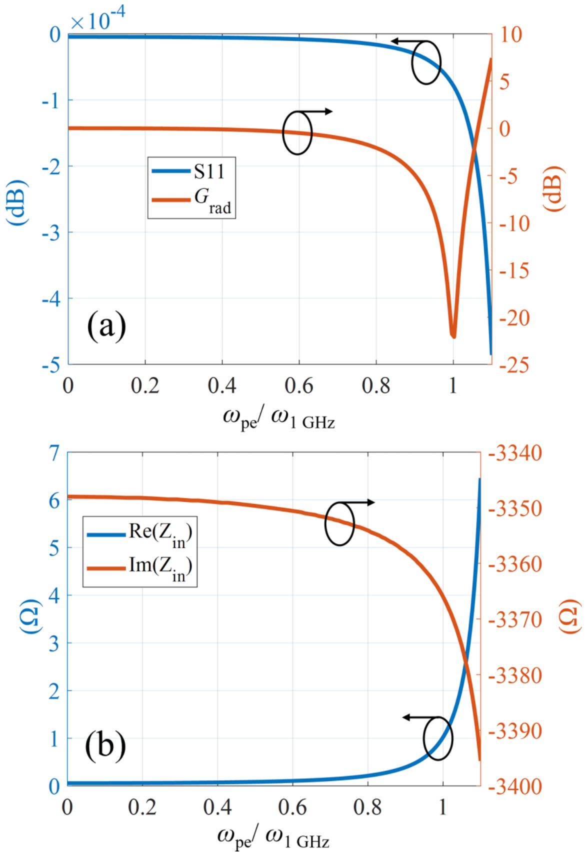

FIG. 6. (a) The radiating gain (G_{rad}, in orange) and the reflection coefficient (S11, in blue); (b) real [Re(Z_{in}), in blue] and imaginary [Im(Z_{in}), in orange] parts of the effective input impedance of an electrically small antenna (ESA) under different $\omega_{\text{pe}}/\omega_{1\text{GHz}}(0 \leqslant \omega_{\text{pe}}/\omega_{1\text{GHz}} \leqslant 1.1)$.

perpendicular to the streamlines, respectively, by fluid dynamics. As a result, when an ENZ plasma is surrounded by two relatively harder EM walls (air), $\mathbf{P}_{\text{av}}$ tends to be restricted in the plasma shell and naturally represents a detour distribution.

B. Radiating mode

For the radiating mode, 3D scattering patterns of the norm of the electric far field, where the normalized plasma frequency $\omega_{\text{pe}}/\omega_{1\text{GHz}} = 0.8083$, 1.0022, or 1.0665, less than, near, or larger than unity, respectively, are shown in Fig. 5. Obviously, the radiating efficiency is omnidirectionally suppressed at the cutoff [Fig. 5(b)] in comparison with those around the cutoff frequency [Figs. 5(a) and 5(c)].

Additionally, the relation between the radiating gain (G_{rad}, in orange) and the reflection coefficient (S11, in blue) of an ESA and its effective input impedance under different $\omega_{\text{pe}}/\omega_{1\text{GHz}}(0 \leqslant \omega_{\text{pe}}/\omega_{1\text{GHz}} \leqslant 1.1)$ are presented in Figs. 6(a) and 6(b), respectively. It can be clearly seen in Fig. 6(a) that, different from G_{rad} with a minimum at $\omega_{\text{pe}}/\omega_{1\text{GHz}} \sim 1$, S11 constantly decreases with a rising $\omega_{\text{pe}}/\omega_{1\text{GHz}}$ of 0 to 1.1. In other words, the far-field radiating power experiences a cutoff, while more EM energy flows out of the feeding source. On the other hand, in Fig. 6(b), one can see that real [Re(Z_{in}), in blue] and imaginary [Im(Z_{in}), in orange] parts of the effective input impedance are positively and negatively proportional to $\omega_{\text{pe}}/\omega_{1\text{GHz}}$, respectively. It is mainly the increase of Re(Z_{in}) that optimizes the matching between an ESA and the transmission line. Next, in the perspective of field interference, we utilized the multipole expansion method [27,28] to analyze the contributions of the antenna and plasma to far-field radiation. Note that only the electric dipole (ED) element is considered in this paper since the size of the plasma shell is sufficiently small compared with the operating wavelength of the ESA (by $r_{\text{out}}/\lambda_{1\text{GHz}} = \frac{1}{15} \ll 1$). Correspondingly, the ED moments of the plasma ($\mathbf{P}^{p}$) and the antenna ($\mathbf{P}^{a}$) are expressed as

$$P^{p}_{r,\varphi,z} = \frac{1}{i\omega}\iiint\limits_{\text{plasma}} J^{p}_{r,\varphi,z}\,dV, \tag{8}$$

$$P^{a}_{r,\varphi,z} = \frac{1}{i\omega}\iint\limits_{\text{antenna}} J^{a}_{r,\varphi,z}\,dS, \tag{9}$$

where $J^{p}_{r,\varphi,z} = i\omega\varepsilon_0(\varepsilon_p - 1)E_{r,\varphi,z}$ is the induced current density of plasma (ε_0 is the vacuum electric permittivity, and E is the electric field), and $J^{a}_{r,\varphi,z}$ is the surface current density along the ESA. On this basis, individual ED contributions of antenna (ED$_a$) and plasma (ED$_p$), as well as the total ED (ED$_t$), to far-field radiation can be obtained by

$$\text{ED}_a = \frac{k_0^4}{12\pi\varepsilon_0^2 c\mu_0}\left(\left|P^{a}_{r}\right|^2 + \left|P^{a}_{\varphi}\right|^2 + \left|P^{a}_{z}\right|^2\right), \tag{10}$$

$$\text{ED}_p = \frac{k_0^4}{12\pi\varepsilon_0^2 c\mu_0}\left(\left|P^{p}_{r}\right|^2 + \left|P^{p}_{\varphi}\right|^2 + \left|P^{p}_{z}\right|^2\right), \tag{11}$$

$$\text{ED}_t = \frac{k_0^4}{12\pi\varepsilon_0^2 c\mu_0}\left(\left|P^{p}_{r} + P^{a}_{r}\right|^2 + \left|P^{p}_{\varphi} + P^{a}_{\varphi}\right|^2 + \left|P^{p}_{z} + P^{a}_{z}\right|^2\right), \tag{12}$$

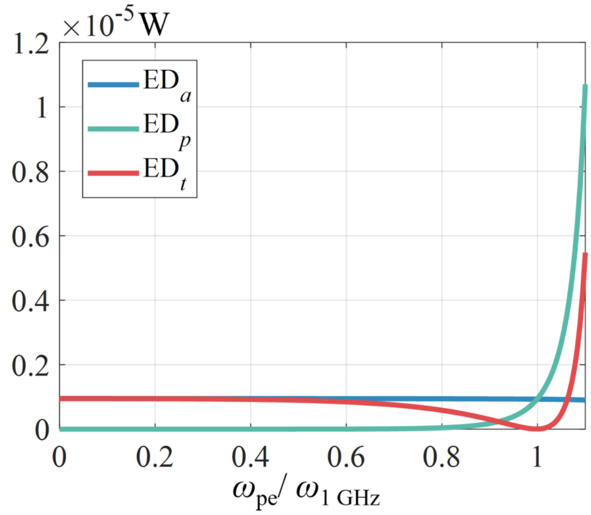

FIG. 7. Electric dipole (ED) contributions of antenna (ED_a, the dark blue line) and plasma (ED_p, the dark green line), as well as total ED (ED_t, the red line), when $0 \leqslant \omega_{\mathrm{pe}}/\omega_{1\mathrm{GHz}} \leqslant 1.1$.

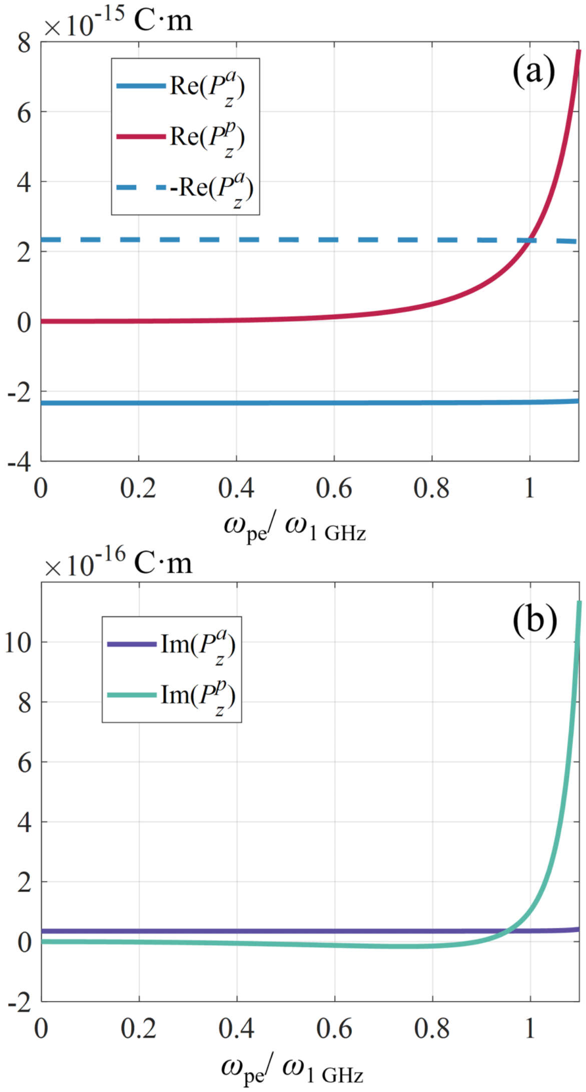

FIG. 8. In the band of $0 \leqslant \omega_{\mathrm{pe}}/\omega_{1\mathrm{GHz}} \leqslant 1.1$, (a) the real part of P_z^a (the solid dark blue line, with $-\mathrm{Re}(P_z^a)$ in dashed dark blue), and the real part of P_z^p (the red line), and (b) the imaginary parts of P_z^a (the purple line) and P_z^p (the dark green line).

where k_0, c, and μ_0 denote the wave number, speed of light, and magnetic permeability in vacuum. Then ED_a, ED_p, and ED_t under different $\omega_{\mathrm{pe}}/\omega_{1\mathrm{GHz}}(0 \leqslant \omega_{\mathrm{pe}}/\omega_{1\mathrm{GHz}} \leqslant 1.1)$ are shown in Fig. 7. It can be observed that ED_p (dark green) is positively proportional to $\omega_{\mathrm{pe}}/\omega_{1\mathrm{GHz}}$, while ED_a (dark blue) is nearly independent of $\omega_{\mathrm{pe}}/\omega_{1\mathrm{GHz}}$. Interestingly, when $\omega_{\mathrm{pe}}/\omega_{1\mathrm{GHz}} \sim 1$, ED_a and ED_p are equal in quantity, while ED_t (red) goes to zero.

It should also be noted that, since the ESA is z polarized, the intensities of ED moments of the ESA and plasma in the z direction are then dominant over other directions. To further reveal the mechanism of the vanishing ED_t at $\omega_{\mathrm{pe}}/\omega_{1\mathrm{GHz}} \sim 1$, we analyzed the real and imaginary parts of P_z^a and P_z^p under different $\omega_{\mathrm{pe}}/\omega_{1\mathrm{GHz}}(0 \leqslant \omega_{\mathrm{pe}}/\omega_{1\mathrm{GHz}} \leqslant 1.1)$, with results shown in Figs. 8(a) and 8(b). One can find that, in the vicinity of the cutoff frequency, the absolute values of the real parts of P_z^a and P_z^p [Fig. 8(a)] are much greater than their imaginary parts [Fig. 8(b)]. In addition, it can be seen in Fig. 8(a) that $-\mathrm{Re}(P_z^a)$ and $\mathrm{Re}(P_z^p)$ intersect at $\omega_{\mathrm{pe}}/\omega_{1\mathrm{GHz}} \sim 1$, where the real parts of P_z^a (solid dark blue) and P_z^p (red) are equal in intensity but with opposite signs. As a result, the far-field radiation is greatly eliminated, as $\mathrm{ED}_t \rightarrow 0$, shown by the red line in Fig. 7, due to the destructive interference of ED fields of the antenna and plasma. In this case, the whole system can be regarded as a nonradiating source [28].

So far, the physical insights of near-field cutoff effects on receiving and radiating have been discussed. However, it should be noticed that the significance of our results is not limited to the theoretical aspect. More broadly, the theory developed here can be applied for explaining practical near-field cutoff situations of receiving and/or radiating and can offer helpful guidance to designing related state-of-the-art micro/nano-optical devices. For instance, Kim *et al.* [29] proposed a technique of electron density diagnosis based on the transmission cutoff of microwave perturbations in plasma, called the wave cutoff method. In the experiment, the length and diameter of the radiating monopole antenna are 5 and 0.1 mm, respectively, and the gap between radiating and detecting antennae is several millimeters. In terms of the working frequency, ranging from 10 kHz to 3 GHz, the cutoff in this case is a typical subwavelength problem. In addition, considering the existence of an ionic sheath between the plasma and the metallic antenna, which can be approximately regarded as a layer of vacuum [30], the wave cutoff method is equivalent to the radiating near-field cutoff. In comparison with Kim's [29] theory that an EM wave is reflected at the cutoff frequency, our explanation is more consistent with the antiresonance transmission line shape observed in experiments.

IV. CONCLUSIONS

To conclude, we have in this paper systematically revealed and distinguished the mechanisms of receiving and radiating near-field cutoff effects based on a subwavelength plasma shell model. It is shown that, for the receiving mode, the ENZ plasma shell resembles a nearly ideal EM fluid where, at the cutoff, time-averaged power flow is mainly transmitted via the plasma shell. As a result, the EM energy that penetrates the internal air space is substantially reduced. In contrast, for the radiating mode, since the ED moments of the antenna and the ENZ plasma in the dominant direction are almost equal in intensity but antiphase, their destructive interference leads to vanishing far-field radiation. Our results may offer opportunities in implementing plasma-based filters, EM shielding devices, and nonradiating sources in the microwave regime and be readily extended to other frequency bands (e.g., terahertz or optical regime) for similar applications.

ACKNOWLEDGMENTS

This paper was supported by the National Natural Science Foundation of China under Grants No. 11875118 and No. 52022026.

[1] B. Wang and M. A. Cappelli, AIP Adv. **6**, 065015 (2016).
[2] J. A. Rodríguez, A. I. Abdalla, B. Wang, B. Lou, S. H. Fan, and M. A. Cappelli, Phys. Rev. Appl. **16**, 014023 (2021).
[3] B. Wang and M. A. Cappelli, Appl. Phys. Lett. **107**, 171107 (2015).
[4] H. J. Yang, S. J. Park, and J. G. Eden, J. Phys. D: Appl. Phys. **50**, 43LT05 (2017).
[5] F. R. Kong, Y. F. Sun, S. Lin, Q. Y. Nie, Z. B. Wang, Z. L. Zhang, B. W. Li, and B. H. Jiang, IEEE Trans. Plasma Sci. **45**, 381 (2017).
[6] V. Laquerbe, R. Pascaud, A. Laffont, T. Callegari, L. Liard, and O. Pascal, Phys. Plasmas **26**, 033509 (2019).
[7] P. Q. Chen, Q. Y. Nie, Z. L. Zhang, B. W. Li, W. S. Li, and X. Ai, Phys. Rev. E **106**, 035207 (2022).
[8] F. F. Chen, *Introduction to Plasma Physics* (Plenum, New York, 1974).
[9] J. H. Kim, D. J. Seong, J. Y. Lim, and K. H. Chung, Appl. Phys. Lett. **83**, 4725 (2003).
[10] C. Laviron, A. J. H. Donné, M. E. Manso, and J. Sanchez, Plasma Phys. Control. Fusion **38**, 905 (1996).
[11] M. Yang, P. Dong, K. Xie, X. P. Li, L. Quan, and J. Li, Phys. Plasmas **28**, 102105 (2021).
[12] A. Ghayekhloo, M. Afsahi, and A. A. Orouji, IEEE Trans. Plasma Sci. **45**, 603 (2017).
[13] H. Singh, S. Antony, and R. M. Jha, *Plasma-Based Radar Cross Section Reduction* (Springer, Singapore, 2016).
[14] Yu. Fedorenko, E. Tereshchenko, S. Pilgaev, V. Grigoryev, and N. Blagoveshchenskaya, Radio Sci. **49**, 1254 (2014).
[15] B. Wang, F. Righetti, and M. A. Cappelli, Phys. Plasmas **25**, 031902 (2018).
[16] M. Silveirinha and N. Engheta, Phys. Rev. Lett. **97**, 157403 (2006).
[17] D. A. Powell, A. Alù, B. Edwards, A. Vakil, Y. S. Kivshar, and N. Engheta, Phys. Rev. B **79**, 245135 (2009).
[18] F. R. Kong, Q. Y. Nie, G. Y. Xu, X. N. Zhang, S. Lin, and B. H. Jiang, Plasma Sci. Technol. **20**, 095504 (2018).
[19] P. Q. Chen, Q. Y. Nie, Z. L. Zhang, B. W. Li, S. Lin, and B. N. Qu, Phys. Plasmas **27**, 053502 (2020).
[20] B. W. Li, Q. Y. Nie, X. G. Wang, S. Lin, P. Q. Chen, and B. N. Qu, Phys. Plasmas **27**, 040701 (2020).
[21] K. M. Chen and C. C. Lin, Proc. IEEE. **56**, 1595 (1968).
[22] C. C. Lin and K. M. Chen, IEEE Trans. Antennas Propag. **17**, 675 (1969).
[23] X. T. Gao, C. S. Wang, B. H. Jiang, and Z. L. Zhang, Phys. Plasmas **21**, 093301 (2014).
[24] C. Pfeiffer and A. Grbic, IEEE Trans. Antennas Propag. **60**, 1671 (2012).
[25] COMSOL Multiphysics, http://www.comsol.com/.
[26] I. Liberal, M. Lobet, Y. Li, and N. Engheta, Proc. Natl. Acad. Sci. USA **117**, 24050 (2020).
[27] A. B. Evlyukhin, T. Fischer, C. Reinhardt, and B. N. Chichkov, Phys. Rev. B **94**, 205434 (2016).
[28] E. Zanganeh, A. Evlyukhin, A. Miroshnichenko, M. Song, E. Nenasheva, and P. Kapitanova, Phys. Rev. Lett. **127**, 096804 (2021).
[29] J. H. Kim, S. C. Choi, Y. H. Shin, and K. H. Chung, Rev. Sci. Instrum. **75**, 2706 (2004).
[30] A. M. Messiaen and P. E. Vandenplas, Electron. Lett. **3**, 26 (1967).